crystals

MDPI

Article

Structural and Optical Properties of $SrTiO_3$-Based Ceramics for Energy and Electronics Applications

Donghoon Kim [1], Soyeon Gwon [1], Kyeongsoon Park [1,*] and Eui-Chan Jeon [2]

[1] Faculty of Nanotechnology and Advanced Materials Engineering, Sejong University, Seoul 05006, Republic of Korea; yy12365@naver.com (D.K.); ksy1013823@naver.com (S.G.)
[2] Department of Climate and Energy, Sejong University, Seoul 05006, Republic of Korea; ecjeon@sejong.ac.kr
* Correspondence: kspark@sejong.ac.kr; Tel.: 82-2-3408-3617; Fax: 82-2-3408-4342

Abstract: A series of $Sr_{1-x}Dy_xTi_{1-y}Nb_yO_{3-\delta}$ ($0.05 \leq x, y \leq 0.10$) samples were fabricated using cold compaction, followed by sintering in a (95% N_2 + 5% H_2) reducing atmosphere. We studied the crystal structure and optical properties of $Sr_{1-x}Dy_xTi_{1-y}Nb_yO_{3-\delta}$ using X-ray diffraction (XRD) with Rietveld refinement, scanning electron microscopy (SEM), X-ray photoelectron spectroscopy (XPS), and ultraviolet−visible−near-infrared (UV-VIS-NIR) spectroscopy. The sintered $Sr_{1-x}Dy_xTi_{1-y}Nb_yO_{3-\delta}$ had a tetragonal structure (*I*4/*mcm* space group). In the sintered samples, Ti ions existed as a mixture of Ti^{3+} and Ti^{4+}, and Nb ions existed as a mixture of Nb^{4+} and Nb^{5+}. The band-gap energies decreased with increasing Dy/Nb concentrations. The incorporation of Ti and Nb ions, the formation of both Ti^{3+} and Nb^{4+} ions, and the reduction in band-gap energies are likely highly effective for increasing the electron concentration and the corresponding electrical conductivity. $Sr_{1-x}Dy_xTi_{1-y}Nb_yO_{3-\delta}$ with high electrical conductivity is suitable for energy and electronics applications.

Keywords: energy; climate change; environment; $SrTiO_3$; crystal structure; structural properties; optical properties; doping

check for updates

Citation: Kim, D.; Gwon, S.; Park, K.; Jeon, E.-C. Structural and Optical Properties of $SrTiO_3$-Based Ceramics for Energy and Electronics Applications. *Crystals* **2024**, *14*, 942. https://doi.org/10.3390/cryst14110942

Academic Editor: Dawei Wang

Received: 19 September 2024
Revised: 28 October 2024
Accepted: 28 October 2024
Published: 30 October 2024

Correction Statement: This article has been republished with a minor change. The change does not affect the scientific content of the article and further details are available within the backmatter of the website version of this article.

Copyright: © 2024 by the authors. Licensee MDPI, Basel, Switzerland. This article is an open access article distributed under the terms and conditions of the Creative Commons Attribution (CC BY) license (https://creativecommons.org/licenses/by/4.0/).

1. Introduction

A perovskite-type metal oxide can be represented by the general formula ABO_3 (A: alkaline earth metal, B: transition metal). Strontium titanate ($SrTiO_3$) at ambient temperature and pressure has a cubic crystal structure (space group $Pm\bar{3}m$, lattice parameter a = 3.905 Å). As the temperature decreases, $SrTiO_3$ undergoes a cubic-to-tetragonal and antiferrodistortive phase transition at approximately 100–110 K [1]. In addition, cubic $SrTiO_3$ consists of corner-shared TiO_6 octahedra surrounding Sr^{2+}, and the Sr^{2+} is bonded to twelve equivalent O^{2-} ions [2–4]. The electronic band structure of $SrTiO_3$ consists of a conduction band formed by triply degenerate Ti 3*d* orbitals and a valence band formed by an O 2*p* orbital [2]. Pure $SrTiO_3$ is an electronic insulator at room temperature [5] but can become an n-type semiconductor by doping donor impurities such as Y, Sm, Nb, and La. Oxygen vacancies can be introduced by heating in a reducing atmosphere or low oxygen partial pressure [1], thereby generating electrons and charged ions. Hence, $SrTiO_3$ is regarded as a mixed electronic–ionic semiconductor.

$SrTiO_3$ possesses several interesting properties, including a high thermoelectric power factor, high chemical and thermal stability, low dielectric loss, a high dielectric constant, high anisotropy, a high melting point (2080 °C), and the generation of photogenerated charge carriers [4–8]. Thus, these characteristics enable a wide range of applications, including thermoelectric materials, anode materials for solid oxide fuel cells (SOFCs), hydrogen sensors, photocatalysts, capacitors, hydrogen storage, solar cells, optical sensors, field effect transistors, random access memory, oxygen sensors, environmental remediation, synaptic emulators, dielectric substrates, and memristors [9–24].

As typical application examples, $SrTiO_3$ possesses a high electron effective mass and Seebeck coefficient due to its degenerate conduction band, leading to excellent thermoelectric performance [9,25,26]. Thermoelectric power generation is a promising technology for addressing global warming and climate change by converting waste heat into electricity. The energy conversion efficiency of thermoelectric materials is measured by the dimensionless figure-of-merit, $ZT = (\sigma\alpha^2/\kappa)T$, where σ, α, κ, and T represent the electrical conductivity, Seebeck coefficient, thermal conductivity, and absolute temperature, respectively. Consequently, increasing the values of σ and α as well as lowering the value of κ value are necessary to enhance the ZT value. In addition, La-doped $SrTiO_3$ has garnered considerable interest as an anode material for SOFCs because of its high electrical conductivity in reducing environments, excellent dimensional and chemical stability during redox cycling, and remarkable resistance to sulfur and coking [11]. SOFCs can help to produce electrical energy and reduce environmental pollution associated with conventional fossil fuels. $SrTiO_3$ can also be used as a photocatalyst to construct photocatalyst panel reactors for evaluating the feasibility of photocatalytic water splitting technology, including the largest panel reactor built for hydrogen production [4,5,13,14].

The electrical conductivity of $SrTiO_3$ increases with donor doping of higher valence cations on Sr and/or Ti sites. Therefore, to further extend the application of $SrTiO_3$ by increasing electrical conductivity, in this work, trivalent Dy^{3+} ions are doped into the Sr^{2+} ion site and pentavalent Nb^{5+} ions are doped into the Ti^{4+} site. Dy/Nb co-doping can enhance the electron concentration in accordance with the following Kröger−Vink equations:

$$Dy_2O_3 + 2Ti_{Ti}^{\times} \overset{SrTiO_3}{\rightarrow} 2Dy_{Sr}^{\bullet} + 2O_O^{\times} + \frac{1}{2}O_2 + 2Ti_{Ti}' \quad (1)$$

$$Nb_2O_5 + 2Ti_{Ti}^{\times} \overset{SrTiO_3}{\rightarrow} 2Nb_{Ti}^{\bullet} + 4O_O^{\times} + \frac{1}{2}O_2 + 2Ti_{Ti}' \quad (2)$$

In the present study, we investigated the crystal structure and optical properties of Dy and Nb co-doped $SrTiO_3$, $Sr_{1-x}Dy_xTi_{1-y}Nb_yO_{3-\delta}$ ($0.05 \leq x, y \leq 0.10$), using SEM, XRD Rietveld refinement, XPS, and optical band-gap energy calculations. XRD Rietveld refinement was performed using FullProf software to retrieve detailed structural parameters. XPS was utilized to examine the oxidation states of the constituting elements (Sr, Dy, Ti, Nb, and O) in $Sr_{1-x}Dy_xTi_{1-y}Nb_yO_{3-\delta}$. UV-Vis-NIR diffuse reflectance spectra were obtained to investigate the optical band-gap energy.

2. Experimental Section

$Sr_{1-x}Dy_xTi_{1-y}Nb_yO_{3-\delta}$ ($0.05 \leq x, y \leq 0.10$) powders were synthesized using a solid-state reaction. The starting powders used were $SrCO_3$ (99.9%), TiO_2 (99.9%, 2 μm), Dy_2O_3 (99.9%), and Nb_2O_5 (99.9%, 1 μm). All the raw materials were purchased from Kojundo Chemical Laboratory Co., Ltd(Osaka, Japan). The starting materials were weighed in specific proportions. A mixture of the weighed starting powders was ball-milled for 8 h at 200 rpm using a ZrO_2 ball as a grinding media. The ball-milled powders were heated to 1300 °C at a heating rate of 5 °C min^{-1} in air, kept at this temperature for 6 h, and then furnace-cooled naturally to room temperature. The resulting powders were milled for 4 h at 350 rpm using a planetary mill (Fritsch Pulverisette 6, Idar-Oberstein, Germany) and ZrO_2 balls. The planetary-milled powders were passed through a 100-mesh sieve and then cold-pressed at 100 MPa to prepare green pellets. The pellets were heated to 1300 °C at a heating rate of 5 °C min^{-1} in a (95% N_2 + 5% H_2) reducing atmosphere, maintained at that temperature for 10 h, and then furnace-cooled to room temperature. The fabricated $Sr_{0.95}Dy_{0.05}Ti_{0.95}Nb_{0.05}O_{3-\delta}$, $Sr_{0.95}Dy_{0.05}Ti_{0.90}Nb_{0.10}O_{3-\delta}$, $Sr_{0.90}Dy_{0.10}Ti_{0.95}Nb_{0.05}O_{3-\delta}$, and $Sr_{0.90}Dy_{0.10}Ti_{0.90}Nb_{0.10}O_{3-\delta}$ samples were designated as D5/N5, D5/N10, D10/N5, and D10/N10, respectively.

The microstructural properties of the sintered samples were examined using a scanning electron microscope (SEM; Hitachi SU8010, Tokyo, Japan). The porosity of the sintered samples was measured using Archimedes' principle. The crystal structure of the sin-

tered samples was analyzed by X-ray diffraction (XRD) at room temperature using an XRD system (X'Pert PRO, PANalytical, Almelo, the Netherlands) with Cu K_α radiation (λ = 1.5406 Å). The crystal structure was further analyzed using XRD Rietveld refinement with the FullProf software. XPS (K−alpha, Thermo VG, Oxford, UK) was employed to examine the surface elemental composition and valence states of the constituent elements in the sintered samples. The optical band-gap of the sintered samples was estimated from the diffuse reflectance spectra measured using a UV−Vis−NIR spectrophotometer (Agilent, Varian Cary 5000, Santa Clara, CA, USA).

3. Results and Discussion

Figure 1 shows the SEM images of $Sr_{1-x}Dy_xTi_{1-y}Nb_yO_{3-\delta}$ ($0.05 \leq x, y \leq 0.10$). The introduction of Dy and Nb ions slightly decreases the bulk density of $Sr_{1-x}Dy_xTi_{1-y}Nb_yO_{3-\delta}$, resulting in 94% and 90% of the theoretical density for the D5/N5 and D10/N10 samples, respectively. Most pores are located at the grain boundaries, which can act as electron scattering centers. As a result, the pores reduce the electrical conductivity (σ), which can be explained by the effective medium theory as follows [27]:

$$\sigma = [(3f - 1)\sigma_0]/2 \quad (3)$$

where f is the fraction of material excluding pores, and σ_0 is the electrical conductivity of pore-free material. Furthermore, the doped Dy and Nb ions reduce the grain size of $Sr_{1-x}Dy_xTi_{1-y}Nb_yO_{3-\delta}$, with grain sizes of 1.3 µm and 0.8 µm for the D5/N5 and D10/N10 samples, respectively. The grain size is estimated using the linear intercept method from the SEM images. The reduction in grain size results from the inhibition of grain boundary mobility due to the pinning effect and solute dragging effect [28,29].

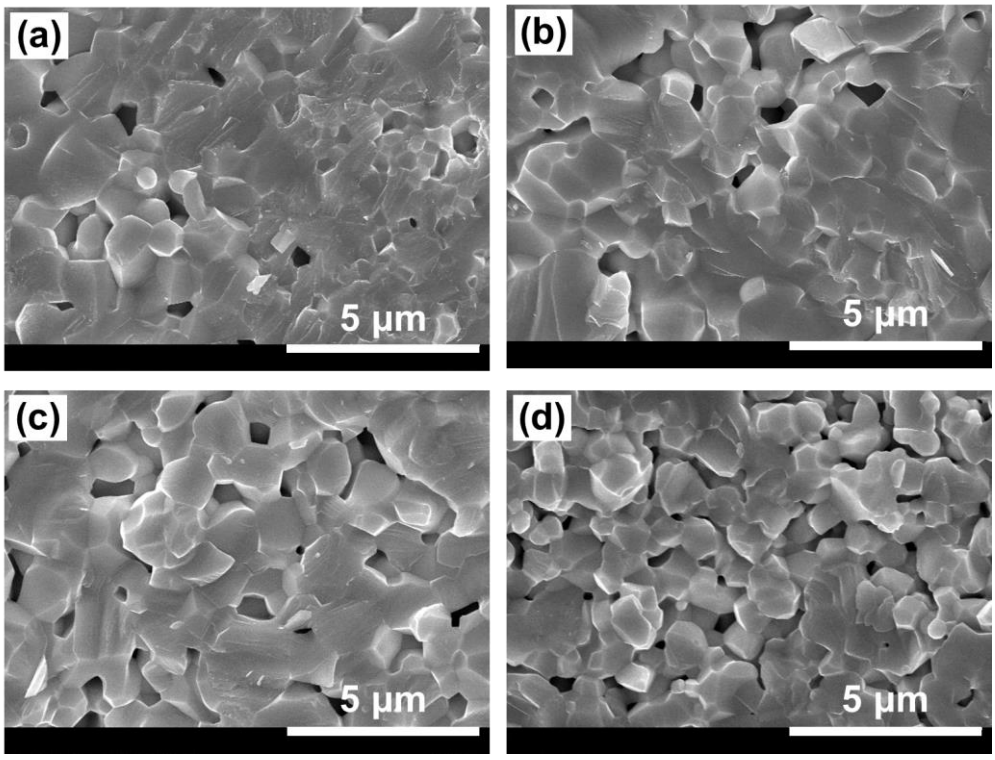


Figure 1. SEM images from the fractured surfaces of the (**a**) D5/N5, (**b**) D5/N10, (**c**) D10/N5, and (**d**) D10/N10 samples.

The standard file of tetragonal $SrTiO_3$ (ICSD # 65140) is employed for the Rietveld refinement. Figure 2 displays the calculated XRD refined profiles of $Sr_{1-x}Dy_xTi_{1-y}Nb_yO_{3-\delta}$ ($0.05 \leq x, y \leq 0.10$) along with the measured diffraction profiles. The diffraction peaks

are indexed as a tetragonal structure with the *I*4/*mcm* space group. Detailed crystallographic information extracted from the refinements and reliability factors (*R* values), including weighted-profile *R* factor (R_{wp}), expected *R* factor (R_{exp}), and goodness of fittings (GOF $\chi = R_{wp}/R_{exp}$), is summarized in Table 1. The lattice parameter decreases with an increasing Dy concentration, whereas it increases with an increasing Nb concentration. The lattice parameters (*a*, *c*) of the D5/N5, D5/N10, D10/N5, and D10/N10 samples are (5.5241 Å, 7.8243 Å), (5.5352 Å, 7.8375 Å), (5.5220 Å, 7.8241 Å), and (5.5336 Å, 7.8374 Å), respectively. This is due to the fact that the ionic radius of Dy^{3+} (1.08 Å) is smaller than that of Sr^{2+} (1.44 Å), while the ionic radius of Nb^{5+} (0.64 Å) is larger than that of Ti^{4+} (0.605 Å) [30,31]. The lattice parameters obtained here are similar to those of previously reported $SrTiO_3$ [32]. The values of R_{wp}, R_{exp}, and χ^2 are in the ranges of 6.23–7.77, 4.17–4.45, and 2.03–3.05, respectively, indicating highly credible Rietveld refinement.

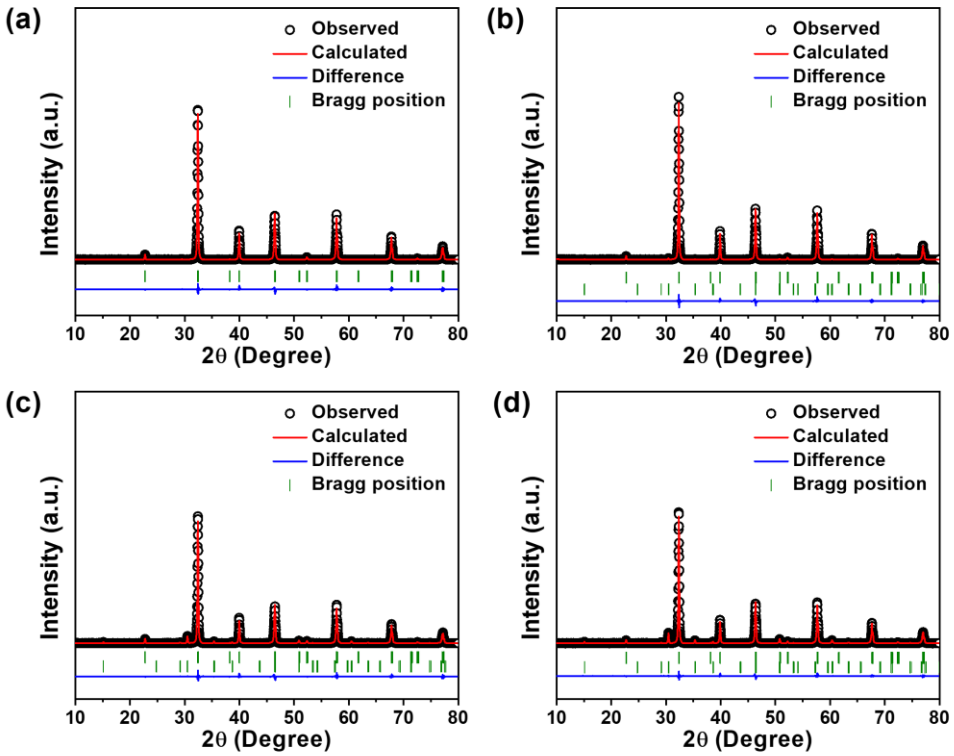


Figure 2. XRD refinement profiles of the (**a**) D5/N5, (**b**) D5/N10, (**c**) D10/N5, and (**d**) D10/N10 samples.

The three-dimensional crystal structures of $Sr_{1-x}Dy_xTi_{1-y}Nb_yO_{3-\delta}$ ($0.05 \leq x, y \leq 0.10$) are generated using the VESTA program and displayed in Supplementary Figure S1. There are two types of oxygen atoms, O(1) and (O2). The bond distances between the constituting atoms of $Sr_{1-x}Dy_xTi_{1-y}Nb_yO_{3-\delta}$ are provided in Table 2. Generally, the bond distances of Sr−O(1), Sr−O(2), Ti−O(1), Ti−O(2), and Ti−Ti for the D5/N5 sample are smaller than those for the D5/N10 sample, whereas the bond distances of Sr−O(1), Sr−O(2), Ti−O(1), Ti−O(2), and Ti−Ti for the D10/N10 sample are larger than those for the D10/N5 sample. This is due to the fact that Dy^{3+} (1.08 Å) has a smaller ionic radius compared to Sr^{2+} (1.44 Å), while Nb^{5+} (0.64 Å) has a larger ionic radius than Ti^{4+} (0.605 Å) [30,31]. The atomic coordinate, isotropic thermal parameter (B_{iso}), and occupancy factor extracted from the Rietveld refinements for $Sr_{1-x}Dy_xTi_{1-y}Nb_yO_{3-\delta}$ are summarized in Supplementary Table S1. The atomic coordinates of Sr, Ti, and O(1) atoms in $Sr_{1-x}Dy_xTi_{1-y}Nb_yO_{3-\delta}$ are scarcely affected by the compositions, specifically (0, 0.50, 0.25), (0, 0, 0), and (0, 0, 0.25), respectively. On the other hand, the atomic coordinates of the O(2) atom are dependent on the compositions, i.e., (0.2281, 0.7281, 0.0000), (0.2304, 0.7304, 0.0000), (0.2220, 0.7220, 0.0000), and (0.2284, 0.7284, 0.0000) for the D5/N5, D5/N10, D10/N5, and D10/N10

samples, respectively. Furthermore, the occupancy factors of the constituting atoms for all the fabricated samples are 1.0000.

Table 1. Crystallographic data and reliability factors of $Sr_{1-x}Dy_xTi_{1-y}Nb_yO_{3-\delta}$ ($0.05 \leq x, y \leq 0.10$).

	D5/N5 sample	D5/N10 sample	D10/N5 sample	D10/N10 sample
Crystal structure	Tetragonal	Tetragonal	Tetragonal	Tetragonal
Space group	*I*4/*mcm*	*I*4/*mcm*	*I*4/*mcm*	*I*4/*mcm*
Lattice parameter				
a (Å)	5.5241	5.5352	5.5220	5.5336
c (Å)	7.8243	7.8375	7.8241	7.8374
$\alpha = \beta = \gamma$ (°)	90.0	90.0	90.0	90.0
Volume (Å^3)	238.76	240.13	238.58	239.99
Reliability factor				
R_{exp} (%)	7.14	6.23	7.77	6.29
R_{exp} (%)	4.17	4.19	4.45	4.41
χ^2	2.94	2.21	3.05	2.03

Table 2. Bond distances between the constituting atoms in $Sr_{1-x}Dy_xTi_{1-y}Nb_yO_{3-\delta}$ ($0.05 \leq x, y \leq 0.10$).

	D5/N5 sample	D5/N10 sample	D10/N5 sample	D10/N10 sample
Sr−O(1) distance (Å)	2.6458	2.6630	2.6139	2.6522
Sr−O(2) distance (Å)	2.7620	2.7676	2.7610	2.7668
Ti−O(1) distance (Å)	1.9561	1.9594	1.9560	1.9645
Ti−O(2) distance (Å)	1.9606	1.9630	1.9645	1.9637
Ti−Ti distance (Å)	3.9061	3.9140	3.9046	3.9128

The oxidation states and binding energies of the constituting elements (Sr, Dy, Ti, Nb, and O) in $Sr_{1-x}Dy_xTi_{1-y}Nb_yO_{3-\delta}$ ($0.05 \leq x, y \leq 0.10$) are investigated using XPS. The survey spectra of $Sr_{1-x}Dy_xTi_{1-y}Nb_yO_{3-\delta}$ in the binding energy range of 0–1350 eV show the presence of the constituting elements and their binding energies (Figure 3). No notable differences are observed among the survey spectra with varying compositions. The binding energies and oxidation states of the Sr, Dy, Ti, Nb, and O elements are obtained from high-resolution XPS scan spectra. In addition to the characteristic peaks of the constituting elements, the C 1s peaks are observed at ~285 eV, indicating the presence of carbon- and oxygen-containing contaminants that typically adsorb onto the sample surface from the atmosphere [33–35]. The adsorbed oxygen may interfere with the O in $Sr_{1-x}Dy_xTi_{1-y}Nb_yO_{3-\delta}$.

The high-resolution XPS scan spectra of the Sr element in the D5/N5 and D10/N10 samples are shown in Figure 4a. The XPS spectra of Sr 3*d* are composed of two peaks, Sr $3d_{3/2}$ and Sr $3d_{5/2}$ [36–38]. The binding energies of the Sr $3d_{3/2}$ and Sr $3d_{5/2}$ peaks are summarized in Supplementary Table S2. The difference between the binding energies of the Sr $3d_{3/2}$ and Sr $3d_{5/2}$ peaks is 1.8 eV, irrespective of the composition. These results indicate that the Sr ions are in the +2 oxidation state. The high-resolution XPS spectra of the Dy element in the D5/N5 and D10/N10 samples are shown in Figure 4b. The symmetrical Dy spectra, centered at ~1296 eV, correspond to Dy $3d_{5/2}$ [39,40], suggesting that the Dy ions are in the +3 oxidation state.

The high-resolution XPS spectra of the Ti element in the D5/N5 and D10/N10 samples are shown in Figure 4c. The XPS spectrum of the D5/N5 sample exhibits characteristic doublet peaks centered at 462.4 and 456.6 eV, which correspond to the Ti^{3+} $2p_{1/2}$ and Ti^{3+} $2p_{3/2}$ peaks, respectively. The binding energies of the Ti $2p_{1/2}$ and Ti $2p_{3/2}$ peaks and the energy separations between these peaks are listed in Supplementary Table S2. The

high-resolution spectra of the Ti ions are deconvoluted to examine their oxidation states. The second set of doublet peaks corresponds to the oxidation state of Ti^{3+} [30]. The Ti^{3+} ions are formed by the partial reduction of Ti^{4+} to Ti^{3+} during sintering in a reducing atmosphere, compensating for the excess electrons introduced by the Dy/Nb co-doping. The relative amounts of the Ti^{3+} and Ti^{4+} ions can be estimated by calculating the ratio of each area of the Ti^{3+} and Ti^{4+} peaks to the total area of the Ti $2p_{1/2}$ and Ti $2p_{3/2}$ peaks. The relative amount of Ti^{3+} increases with an increasing Dy/Nb concentration, reaching 12% and 20% for the D5/N5 and D10/N10 samples, respectively (Supplementary Table S3). These findings indicate that the Ti ions are in a mixed oxidation state (+3 and +4), with the major oxidation state being +4 [30,41–46]. The formation of trivalent Ti^{3+} can generate additional electrons.

The high-resolution XPS spectra of the Nb element in the D5/N5 and D10/N10 samples are shown in Figure 4d. The XPS spectra of Nb 3*d* consist of Nb $3d_{5/2}$ and Nb $3d_{3/2}$ spin−orbit doublets [30]. In the D5/N5 sample, the binding energies of Nb^{4+} $3d_{3/2}$ and $3d_{5/2}$ peaks are located at 208.5 and 205.7 eV, respectively, while those of Nb^{5+} $3d_{3/2}$ and $3d_{5/2}$ peaks are located at 209.4 and 206.7 eV, respectively (Supplementary Table S2). The Nb ions exist as a mixture of Nb^{4+} and Nb^{5+}. The relative amounts of the Nb^{4+} and Nb^{5+} ions are presented in Supplementary Table S3. As the Dy/Nb concentration increases, the relative amount of Nb^{4+} rises from 8% in the D5/N5 sample to 10% in the D10/N10 sample. The formation of both Ti^{3+} and Nb^{4+} ions in $Sr_{1-x}Dy_xTi_{1-y}Nb_yO_{3-\delta}$ can increase the electron concentration of the system, in accordance with the Kröger−Vink equations discussed previously in Equations (1) and (2), thereby enhancing electrical conductivity. The electrical conductivity (σ) can be expressed as $\sigma = ne\mu$, where n is the electron concentration, e is the electronic charge, and μ is the electron mobility. The electron concentration and electrical conductivity of $Sr_{1-x}Dy_xTi_{1-y}Nb_yO_{3-\delta}$ are provided in our previous report [47].

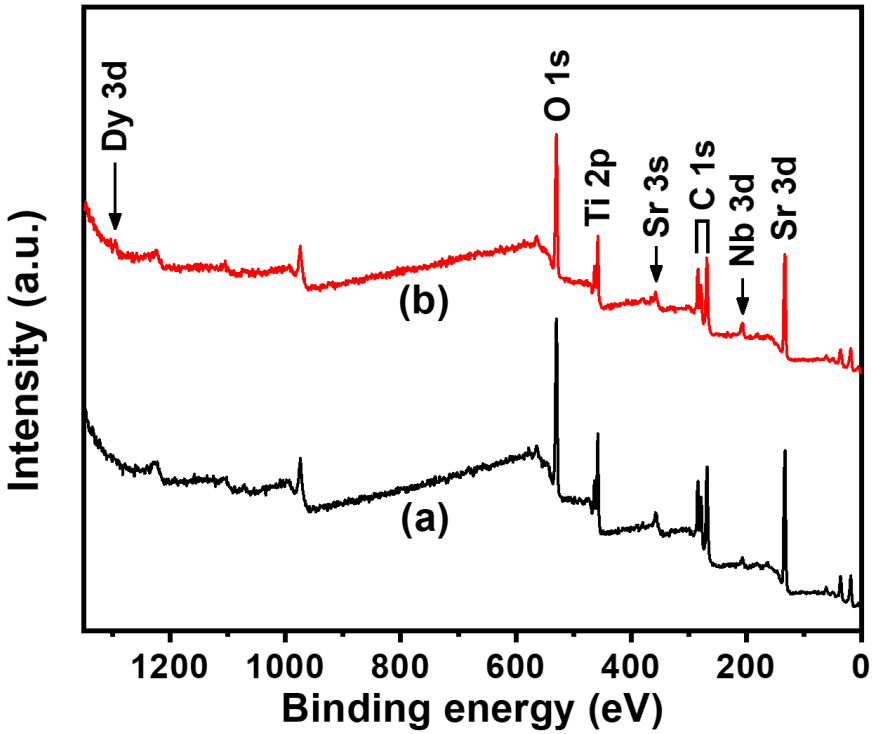


Figure 3. XPS survey spectra of the (**a**) D5/N5 and (**b**) D10/N10 samples.

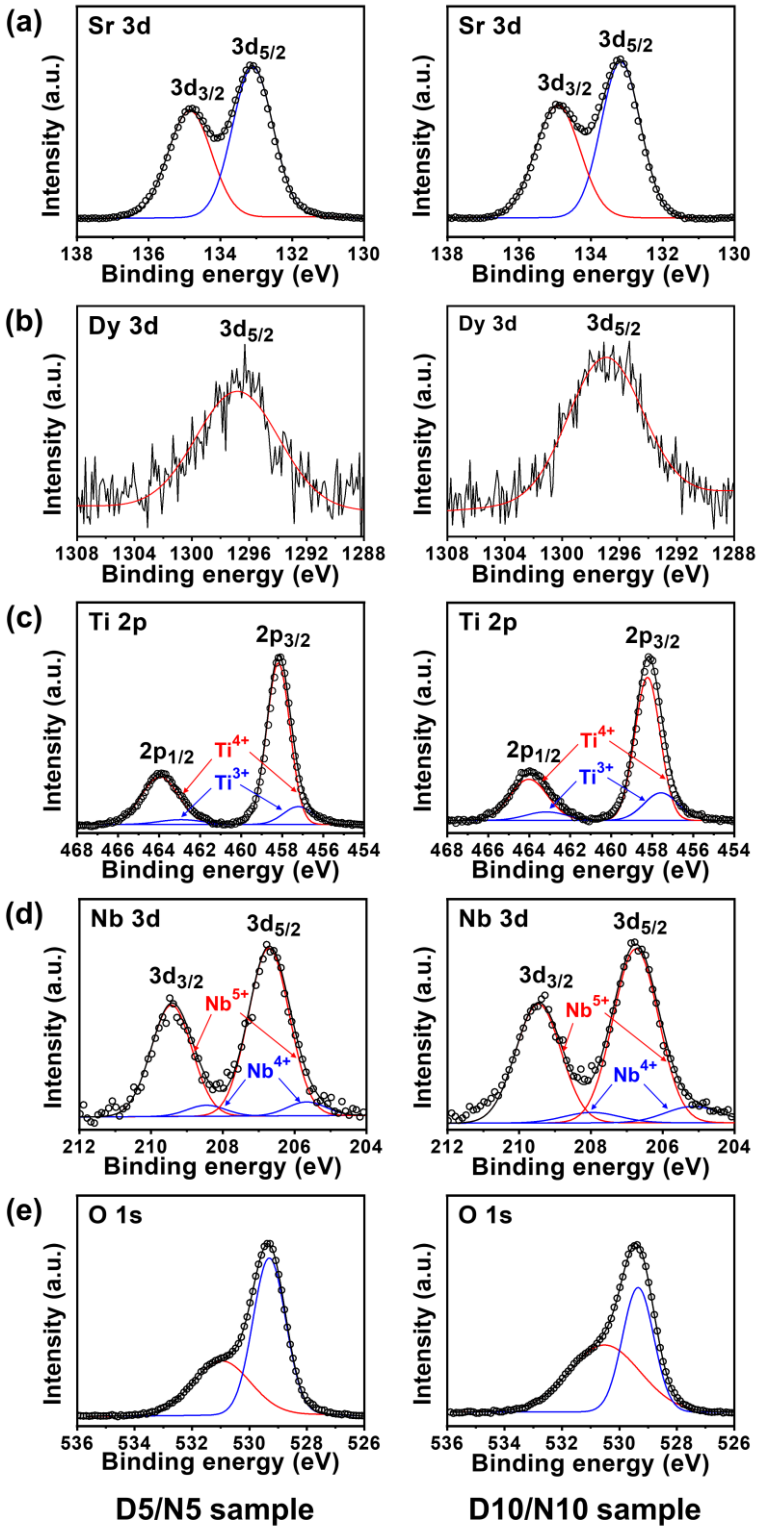


Figure 4. High-resolution XPS spectra of the (**a**) Sr, (**b**) Dy, (**c**) Ti, (**d**) Nb, and (**e**) O elements in the D5/N5 and D10/N10 samples.

The high-resolution XPS spectra of the O element in the D5/N5 and D10/N10 samples are shown in Figure 4e. The O 1s spectra of the D5/N5 sample can be decomposed into two distinct peaks at 531.1 eV and 529.3 eV, which are associated with surface-adsorbed or non-lattice oxygen and lattice oxygen bonded with titanium (Ti−O), respectively [48,49]. The O 1s corresponds to an oxidation state of −2.

To investigate the optical band-gap energy of $Sr_{1-x}Dy_xTi_{1-y}Nb_yO_{3-\delta}$ ($0.05 \leq x, y \leq 0.10$), the UV−Vis−NIR diffuse reflectance spectra are obtained, as shown in Figure 5a. The diffuse reflectance substantially increases with increasing wavelength in the wavelength of 350 to 400 nm. It has been reported that $SrTiO_3$ is an indirect semiconductor [50,51]. Therefore, the band-gap energy (E_g) of $Sr_{1-x}Dy_xTi_{1-y}Nb_yO_{3-\delta}$ can be calculated using the relation $(\alpha h\nu)^{1/2} = A(h\nu - E_g)$ [52], where α is the absorption coefficient, ν is the photon frequency, h is the Planck constant, E_g is the optical band-gap energy, and A is a proportionality constant. The band-gap energy (E_g) of all the samples is obtained by extrapolating the linear part to $(\alpha h\nu)^{1/2} = 0$, as represented in Figure 5b. The band-gap energies slightly decrease with increasing Dy/Nb concentrations, e.g., 2.9 and 2.7 eV for the D5/N5 and D10/N10 samples, respectively (Table 3). Furthermore, the band-gap energies of the prepared $Sr_{1-x}Dy_xTi_{1-y}Nb_yO_{3-\delta}$ are smaller than those of previously reported pristine $SrTiO_3$ (~3.2 eV) [52,53]. The narrowing of band-gap energy is beneficial for enhancing the electron concentration due to the increased excitation of electrons from the valence to conduction band.

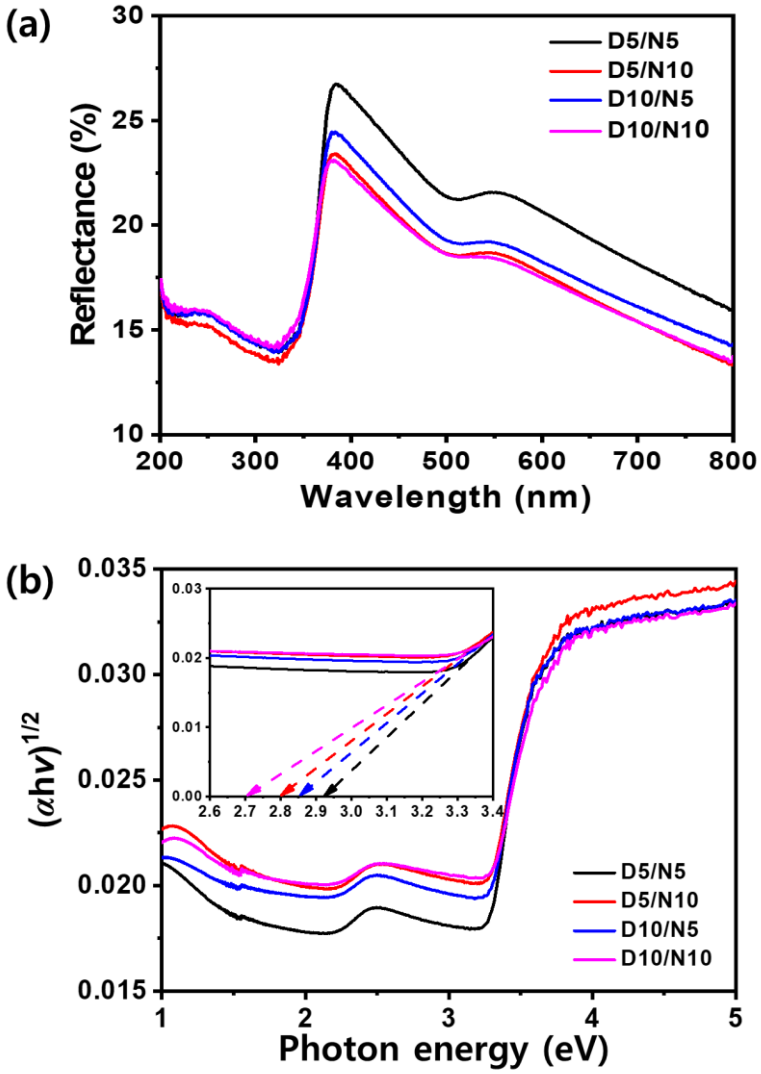


Figure 5. (**a**) UV−Vis−NIR diffuse reflectance spectra and (**b**) relationship between $(\alpha h\nu)^{1/2}$ and photon energy ($h\nu$) of $Sr_{1-x}Dy_xTi_{1-y}Nb_yO_{3-\delta}$ ($0.05 \leq x, y \leq 0.10$).

Table 3. Band-gap energy of $Sr_{1-x}Dy_xTi_{1-y}Nb_yO_{3-\delta}$ ($0.05 \leq x, y \leq 0.10$).

	D5/N5 sample	D5/N10 sample	D10/N5 sample	D10/N10 sample
Band-gap energy (eV)	2.9	2.8	2.8	2.7

4. Conclusions

$Sr_{1-x}Dy_xTi_{1-y}Nb_yO_{3-\delta}$ ($0.05 \leq x, y \leq 0.10$) samples were fabricated using cold compaction, followed by sintering in a (95% N_2 + 5% H_2) reducing atmosphere. $Sr_{1-x}Dy_xTi_{1-y}Nb_yO_{3-\delta}$ had a tetragonal structure (*I*4/*mcm* space group). Ti ions in the sintered samples existed as a mixture of Ti^{3+} and Ti^{4+}, and Nb ions existed as a mixture of Nb^{4+} and Nb^{5+}. The major valences of Ti and Nb ions were +4 and +5, respectively. The incorporation of Ti and Nb ions into $SrTiO_3$ reduced the band-gap energies. The incorporation of Ti and Nb ions, the formation of both Ti^{3+} and Nb^{4+} ions, and the reduction in band-gap energies can effectively increase the electron concentration and its corresponding electrical conductivity. We believe that $Sr_{1-x}Dy_xTi_{1-y}Nb_yO_{3-\delta}$ with high electrical conductivity can be utilized in energy and electronics applications.

Supplementary Materials: The following supporting information can be downloaded at: https://www.mdpi.com/article/10.3390/cryst14110942/s1, Figure S1: Crystal structures of the (a) D5/N5, (b) D5/N10, (c) D10/N5, and (d) D10/N10 samples.; Table S1: Atomic coordinate, thermal parameter Biso, and occupancy factor of $Sr_{1-x}Dy_xTi_{1-y}Nb_yO_{3-\delta}$ ($0.05 \leq x, y \leq 0.10$); Table S2: Binding energies of the constituting elements (Sr, Dy, Ti, Nb, and O) in $Sr_{1-x}Dy_xTi_{1-y}Nb_yO_{3-\delta}$ ($0.05 \leq x, y \leq 0.10$). Table S3: Relative amounts of the Ti_{3+}/Ti_{4+} and the Nb_{4+}/Nb_{5+} in $Sr_{1-x}Dy_xTi_{1-y}Nb_yO_{3-\delta}$ ($0.05 \leq x, y \leq 0.10$).

Author Contributions: Conceptualization, D.K., S.G., E.-C.J. and K.P.; methodology, D.K. and S.G.; formal analysis, D.K.; investigation, S.G.; writing—original draft preparation, D.K. and K.P.; writing—review and editing, K.P.; supervision, E.-C.J.; project administration, K.P.; funding acquisition, E.-C.J. All authors have read and agreed to the published version of the manuscript.

Funding: This work is financially supported by Korea Ministry of Environment (MOE) as Graduate School specialized in Climate Change.

Data Availability Statement: The original contributions presented in the study are included in the article/Supplementary Materials, further inquiries can be directed to the corresponding author/s.

Conflicts of Interest: The authors declare no conflict of interest.

References

1. Pai, Y.Y.; Tylan–Tyler, A.; Irvin, P.; Levy, J. Physics of $SrTiO_3$-based heterostructures and nanostructures: A review. *Rep. Prog. Phys.* **2018**, *81*, 036503. [CrossRef] [PubMed]
2. Chen, P.; Cosgriff, M.P.; Zhang, Q.; Callori, S.J.; Adams, B.W.; Dufresne, E.M.; Dawber, M.; Evans, P.G. Field–dependent domain distortion and interlayer polarization distribution in $PbTiO_3/SrTiO_3$ superlattices. *Phys. Rev. Lett.* **2013**, *110*, 047601. [CrossRef]
3. Neaton, J.; Rabe, K. Theory of polarization enhancement in epitaxial $BaTiO_3/SrTiO_3$ superlattices. *Appl. Phys. Lett.* **2003**, *82*, 1586–1588. [CrossRef]
4. Avcıoğlu, C.; Avcıoğlu, S.; Bekheet, M.F.; Gurlo, A. Photocatalytic overall water splitting by $SrTiO_3$: Progress report and design strategies. *ACS Appl. Energy Mater.* **2023**, *6*, 1134–1154. [CrossRef]
5. Phoon, B.L.; Lai, C.W.; Juan, J.C.; Show, P.L.; Chen, W.H. A review of synthesis and morphology of $SrTiO_3$ for energy and other applications. *Int. J. Energy Res.* **2019**, *43*, 5151–5174. [CrossRef]
6. Koumoto, K.; Wang, Y.F.; Zhang, R.Z.; Kosuga, A.; Funahashi, R. Oxide thermoelectric materials: A nanostructuring approach. *Annu. Rev. Mater. Res.* **2010**, *40*, 363–394. [CrossRef]
7. Li, Y.; Triveno, G.B.; Lin, X.; Guan, P.; Chu, D. Morphology control and applications of $SrTiO_3$ based nanomaterials. *Curr. Phys. Chem.* **2017**, *7*, 191–203. [CrossRef]
8. Ekuma, C.E.; Jarrell, M.; Moreno, J.; Bagayoko, D. First principle electronic, structural, elastic, and optical properties of strontium titanate. *AIP Adv.* **2012**, *2*, 012189. [CrossRef]
9. Zhang, B.; Wang, J.; Zou, T.; Zhang, S.; Yaer, X.; Ding, N.; Liu, C.; Miao, L.; Li, Y.; Wu, Y. High thermoelectric performance of Nb-doped $SrTiO_3$ bulk materials with different doping levels. *J. Mater. Chem. C.* **2015**, *3*, 11406–11411.

10. Shen, X.; Kawabata, T.; Sasaki, K. Redox-stable $Sr_{0.9}La_{0.1}TiO_3$-supported SOFC single cells. *Int. J. Hydrogen Energy* **2017**, *42*, 6941–6949. [CrossRef]
11. Zhou, X.; Yan, N.; Chuang, K.T.; Luo, J. Progress in La–doped $SrTiO_3$ (LST)-based anode materials for solid oxide fuel cells. *RSC Adv.* **2014**, *4*, 118–131. [CrossRef]
12. Schultz, A.M.; Brown, T.D.; Ohodnicki, P.R., Jr. Optical and chemi–resistive sensing in extreme environments: La–doped $SrTiO_3$ films for hydrogen sensing at high temperatures. *J. Phys. Chem. C* **2015**, *119*, 6211–6220. [CrossRef]
13. Xu, Y.; Liang, Y.; Hei, Q.; Xui, R.; Chen, D.; Xu, X.; Hu, H. Review of doping $SrTiO_3$ for photocatalytic applications. *Bull. Mater. Sci.* **2023**, *46*, 6. [CrossRef]
14. Qin, Y.; Fang, F.; Xie, Z.; Lin, H.; Zhang, K.; Yu, X.; Chang, K. La, Al–codoped $SrTiO_3$ as a photocatalyst in overall water splitting: Significant surface engineering effects on defect engineering. *ACS Catal.* **2021**, *11*, 11429–11439. [CrossRef]
15. Yahya, M.; Ismail, M. Catalytic effect of $SrTiO_3$ on the hydrogen storage behaviour of MgH_2. *J. Energy Chem.* **2019**, *28*, 46–53. [CrossRef]
16. Gholamrezaei, S.; Salavati-Niasari, M. Natural sensitizer for low cost dye sensitized solar cell based on strontium titanate nanoparticles. *J. Mat. Sci. Mat. Electr.* **2016**, *27*, 2467–2472. [CrossRef]
17. Chen, C.; Dai, Q.; Miao, C.; Xu, L.; Song, H. Strontium titanate nanoparticles as the photoanode for CdS quantum dot sensitized solar cells. *RSC Adv.* **2015**, *5*, 4844–4852. [CrossRef]
18. Popovici, M.; Swerts, J.; Redolfi, A.; Kaczer, B.; Aoulaiche, M.; Radu, I.; Clima, S.; Everaert, J.L.; Van Elshocht, S.; Jurczak, M. Low leakage Ru-strontium titanate–Ru metal–insulator–metal capacitors for sub-20 nm technology node in dynamic random access memory. *Appl. Phy. Lett.* **2014**, *104*, 082908. [CrossRef]
19. Tang, H.; Sodano, H.A. Ultra high energy density nanocomposite capacitors with fast discharge using $Ba_{0.2}Sr_{0.8}TiO_3$ nanowires. *Nano Lett.* **2013**, *13*, 1373–1379. [CrossRef]
20. Tarun, M.C.; Selim, F.A.; McCluskey, M.D. Persistent photoconductivity in strontium titanate. *Phys. Rev. Lett.* **2013**, *111*, 187403. [CrossRef]
21. Chow, C.L.; Tan, P.Y.; Tan, O.K.; Tse, M.S.; Phuan, Y.S. Oxygen sensing properties of strontium titanate ferrite composite films at low temperature. *Sensor Lett.* **2011**, *9*, 343–347. [CrossRef]
22. Nie, F.; Wang, J.; Fang, H.; Ma, S.; Wu, F.; Zhao, W.; Wei, S.; Wang, Y.; Zhao, L.; Yan, S. Ultrathin $SrTiO_3$-based oxide memristor with both drift and diffusive dynamics as versatile synaptic emulators for neuromorphic computing. *Mater. Futures* **2023**, *2*, 035302. [CrossRef]
23. Lu, J.; Deng, Z.; Ye, Q.; Zheng, Z.; Yao, J.; Yang, G. Promoting the performance of 2D material photodetectors by dielectric engineering. *Small Methods* **2022**, *6*, 210104. [CrossRef]
24. Ho, T.L.; Ding, K.; Lyapunov, N.; Suen, C.H.; Wong, L.W.; Zhao, J.; Yang, M.Y.; Zhou, X.; Dai, J.Y. Multi-level resistive switching in SnSe/$SrTiO_3$ heterostructure based memristor device. *Nanomaterials* **2022**, *12*, 2128. [CrossRef]
25. Ohta, S.; Nomura, T.; Ohta, H.; Koumoto, K. High-temperature carrier transport and thermoelectric properties of heavily La- or Nb-doped $SrTiO_3$ single crystals. *J. Appl. Phys.* **2005**, *9*, 034106.
26. Okuda, T.; Nakanishi, K.; Miyasaka, S.; Tokura, Y. Large thermoelectric response of metallic perovskites: $Sr_{1-x}La_xTiO_3$ ($0 < x < 0.1$). *Phys. Rev. B* **2001**, *63*, 113104.
27. Yoon, S.; Kwon, O.J.; Ahn, S.; Kim, J.Y.; Koo, H.; Bae, S.H.; Cho, J.Y.; Kim, J.S.; Park, C. The effect of grain size and density on the thermoelectric properties of Bi_2Te_3-PbTe compounds. *J. Electron. Mater.* **2013**, *42*, 3390–3396. [CrossRef]
28. Bernik, S.; Daneu, N.; Rečnik, A. Inversion boundary induced grain growth in TiO_2 or Sb_2O_3 doped ZnO-based varistor ceramics. *J. Eur. Ceram. Soc.* **2004**, *24*, 3703–3708. [CrossRef]
29. Jin, Z.; Yu, D.; Wu, X.; Yin, K.; Yan, K. Drag effects of solute and second phase distributions on the grain growth kinetics of pre-extruded Mg-6Zn alloy. *J. Mater. Sci. Technol.* **2016**, *32*, 1260–1266. [CrossRef]
30. Li, Y.; Hou, Q.Y.; Wang, X.H.; Kang, H.J.; Yaer, X.; Li, J.B.; Wang, T.M.; Miao, L.; Wang, J. First-principles calculations and high thermoelectric performance of La-Nb doped $SrTiO_3$ ceramics. *J. Mater. Chem. A* **2019**, *7*, 236–247. [CrossRef]
31. Wang, H.C.; Wang, C.L.; Su, W.B.; Liu, J.; Sun, Y.; Peng, H.; Mei, L.M. Doping effect of La and Dy on the thermoelectric properties of $SrTiO_3$. *J. Am. Ceram. Soc.* **2011**, *94*, 838–842. [CrossRef]
32. Evarestov, R.A.; Blokhin, E.; Gryaznov, D.; Kotomin, E.A.; Maier, J. Phonon calculations in cubic and tetragonal phases of $SrTiO_3$: A comparative LCAO and plane–wave study. *Phys. Rev. B* **2011**, *83*, 134108. [CrossRef]
33. Pronin, I.A.; Averin, I.A.; Karmanov, A.A.; Yakushova, N.D.; Komolov, A.S.; Lazneva, E.F.; Sychev, M.M.; Moshnikov, V.A.; Korotcenkov, G. Control over the surface properties of zinc oxide powders via combining mechanical, electron beam, and thermal processing. *Nanomaterials* **2022**, *12*, 1924. [CrossRef] [PubMed]
34. Komolov, A.S.; Lazneva, E.F.; Gerasimova, N.B.; Panina, Y.A.; Sobolev, V.S.; Koroleva, A.V.; Pshenichnyuk, S.A.; Asfandiarov, N.L.; Modelli, A.; Handke, B.; et al. Conduction band electronic states of ultrathin layers of thiophene/ phenylene co-oligomers on an oxidized silicon surface. *J. Electron Spectrosc. Relat. Phenom.* **2019**, *235*, 40–45. [CrossRef]
35. Comini, N.; Huthwelker, T.; Diulus, J.T.; Osterwalder, J.; Novotny, Z. Factors influencing surface carbon contamination in ambient-pressure X-ray photoelectron spectroscopy experiments. *J. Vac. Sci. Technol. A* **2021**, *39*, 043203. [CrossRef]
36. Wu, Q.H.; Liu, M.; Jaegermann, W. X-ray photoelectron spectroscopy of $La_{0.5}Sr_{0.5}MnO_3$. *Mater. Lett.* **2005**, *59*, 1980–1983. [CrossRef]

37. Shichi, Y.; Inoue, Y.; Munakata, F.; Yamanaka, M. X-ray photoelectron spectroscopy analysis of $Bi_2Sr_2Ca_{1-x}Y_xCu_2O_y$. *Phys. Rev. B* **1990**, *42*, 939–942. [CrossRef]
38. Márquez–Herrera, A.; Ovando–Medina, V.M.; Castillo-Reyes, B.E.; Zapata–Torres, M.; Meléndez–Lira, M.; González–Castañeda, J. Facile synthesis of $SrCO_3$-$Sr(OH)_2$/PPy nanocomposite with enhanced photocatalytic activity under visible light. *Materials* **2016**, *9*, 30. [CrossRef]
39. Jung, J.; Kim, J.; Shim, Y.S.; Hwang, D.; Son, C.S. Structure and photoluminescence properties of rare–earth (Dy^{3+}, Tb^{3+}, Sm^{3+})-doped $BaWO_4$ phosphors synthesized via co–precipitation for anti–counterfeiting. *Materials* **2020**, *13*, 4165. [CrossRef]
40. Munirathnam, K.; Dillip, G.R.; Chaurasia, S.; Joo, S.W.; Raju, D.P.; Sushmae, N.J. Investigations on surface chemical analysis using X–ray photoelectron spectroscopy and optical properties of Dy^{3+}-doped $LiNa_3P_2O_7$ phosphor. *J. Mol. Struct.* **2016**, *1118*, 117–123. [CrossRef]
41. Atuchin, V.V.; Gavrilova, T.A.; Grivel, J.C.; Kesler, V.G.; Troitskaia, I.B. Electronic structure of layered ferroelectric high-k titanate $Pr_2Ti_2O_7$. *J. Solid State Chem.* **2012**, *195*, 125–131. [CrossRef]
42. Thind, S.S.; Wu, G.; Tian, M.; Chen, A. Significant enhancement in the photocatalytic activity of N, W co–doped TiO_2 nanomaterials for promising environmental applications. *Nanotechnology* **2012**, *23*, 475706. [CrossRef] [PubMed]
43. Luciu, I.; Bartali, R.; Laidani, N. Influence of hydrogen addition to an Ar plasma on the structural properties of TiO_{2-x} thin films deposited by RF sputtering. *J. Phys. D* **2012**, *45*, 345302. [CrossRef]
44. Kovalevsky, A.V.; Populoh, S.; Patrício, S.G.; Thiel, P.; Ferro, M.C.; Fagg, D.P.; Frade, J.R.; Weidenkaff, A. Design of $SrTiO_3$-based thermoelectrics by tungsten substitution. *J. Phys. Chem. C* **2015**, *119*, 4466–4478. [CrossRef]
45. Ekren, D.; Azough, F.; Gholinia, A.; Day, S.J.; Hernandez–Maldonado, D.; Kepaptsoglou, D.M.; Ramasse, Q.M.; Freer, R. Enhancing the thermoelectric power factor of $Sr_{0.9}Nd_{0.1}TiO_3$ through control of the nanostructure and microstructure. *J. Mater. Chem. A* **2018**, *6*, 24928–24939. [CrossRef]
46. Liu, D.Q.; Zhang, Y.W.; Kang, H.J.; Li, J.L.; Yang, X.; Wang, T.M. Effect of Nb doping on microstructures and thermoelectric properties of $SrTiO_3$ ceramics. *Chin. Phys. B* **2018**, *27*, 047205. [CrossRef]
47. Park, K.; Kim, D.H.; Gwon, S.Y.; Jeon, E.C. High thermoelectric performance of n–type $SrTiO_3$ by Dy and Nb co-doping. *Inorg. Chem. Comm.* **2024**, *169*, 113041. [CrossRef]
48. Zhang, H.; Guashuai, M.; Xingping, M.; Bei, W. Fabrication and photocatalytic property of one–dimensional $SrTiO_3/TiO_{2-x}N_x$ nanostructures. *Int. J. Photoenergy* **2013**, *2013*, 1–6.
49. Devi, N.Y.; Rajasekaran, P.; Vijayakumar, K.; Nedunchezhian, A.S.A.; Sidharth, D.; Anbalagan, G.; Arivanandhan, M.; Jayavel, R. Enhancement of thermoelectric power factor of hydrothermally synthesised $SrTiO_3$ nanostructures. *Mater. Res. Exp.* **2020**, *7*, 015094. [CrossRef]
50. Kok, D.J.; Irmscher, K.; Naumann, M.; Guguschev, C.; Galazka, Z.; Uecker, R. Temperature–dependent optical absorption of $SrTiO_3$. *Phys. Status Solidi A* **2015**, *212*, 1880–1887. [CrossRef]
51. Makuła, P.; Pacia, M.; Macyk, W. How to correctly determine the band gap energy of modified semiconductor photocatalysts based on UV–Vis spectra. *J. Phys. Chem. Lett.* **2018**, *9*, 6814–6817. [CrossRef]
52. Mochizuki, S.; Fujishiro, F.; Minami, S. Photoluminescence and reversible photo–induced spectral change of $SrTiO_3$. *J. Phys. Condens. Matter* **2005**, *17*, 923–948. [CrossRef]
53. Yamada, Y.; Kanemitsu, Y. Band-to-band photoluminescence in $SrTiO_3$. *Phys. Rev. B* **2010**, *82*, 121103. [CrossRef]

Disclaimer/Publisher's Note: The statements, opinions and data contained in all publications are solely those of the individual author(s) and contributor(s) and not of MDPI and/or the editor(s). MDPI and/or the editor(s) disclaim responsibility for any injury to people or property resulting from any ideas, methods, instructions or products referred to in the content.